(Received 23 May 2025, Accepted 3 August 2025, Scheduled 11 August 2025)

Global Designed Angle-Multiplexed Metasurface for Holographic Imaging Enabled by the Diffractive Neural Network

Dashuang Liao[1, 2, 3], Chan Wang[2, 3], Xiaokang Zhu[2, 3], Liqiao Jing[2, 3, *], Min Li[4, *], and Zuojia Wang[2, 3, *]

[1] *Department of Computer Science, Anhui Medical University, Hefei 230032, China*
[2] *Interdisciplinary Center for Quantum Information, State Key Laboratory of Modern Optical Instrumentation ZJU-Hangzhou Global Scientific and Technological Innovation Center, Zhejiang University, Hangzhou 310027, China*
[3] *International Joint Innovation Center Zhejiang Key Laboratory of Intelligent Electromagnetic Control and Advanced Electronic Integration The Electromagnetics Academy at Zhejiang University, Zhejiang University, Haining 314400, China*
[4] *Anhui Provincial Engineering Research Center for Agricultural Information Perception and Intelligent Computing & Anhui Provincial Key Laboratory of Smart Agricultural Technology and Equipment, Anhui Agricultural University, Hefei 310026, China*

ABSTRACT: Diffractive optical elements, including holograms and metasurfaces, are widely employed in imaging, display, and information processing systems. To enhance information capacity, various multiplexing techniques such as wavelength, polarization, and spatial multiplexing have been extensively explored. However, the angular optical memory effect induces strong correlations in the diffracted output under varying angles of incidence, thereby fundamentally limiting the use of illumination angle as an independent degree of freedom in multiplexing strategies. Here, we propose and experimentally demonstrate a globally designed angle-multiplexed metasurface hologram enabled by a diffractive neural network (DNN). Angular multiplexing in the DNN is realized by harnessing illumination angle-dependent phase delays across local units, rather than relying on complex local designs with intrinsic angular dispersion. The DNN is trained using complex electric field distributions and corresponding target images for each incident angle, enabling end-to-end optimization of the entire metasurface phase profile to encode multiple angular channels simultaneously. Besides, phase modulation of circularly polarized transmitted waves is achieved via geometric phase engineering, using a single-layer and fabrication-compatible meta-atom design without relying on multilayer stacking or inter-resonator coupling. Experimental measurements validate the high-fidelity reconstruction of both images at their respective angles, consistent with numerical simulations. Furthermore, robustness studies confirm that the proposed metasurface can tolerate reasonable variations in incident magnitude, angle, and frequency, as well as fabrication-induced phase errors, while preserving imaging fidelity. The proposed metasurface and design strategy offer a scalable platform for high-density information encoding and multiplexed optical systems, with potential applications in augmented reality, secure communication, and multi-view display technologies.

1. INTRODUCTION

Metasurfaces, the two-dimensional (2D) counterparts of bulky metamaterials, have attracted an explosion of interest and witnessed a rapid development in both academia and industry, due to the unprecedented flexibility in manipulating the amplitude, phase, and polarization of electromagnetic (EM) waves at the subwavelength scale. Their versatile design freedom and integrability have enabled a broad range of transformative applications across the electromagnetic spectrum, such as invisibility cloaks [1–3], polarization converters [4], vortex beam generators [5, 6], meta-holograms [7, 8], meta-antennas [9, 10], and chiral perfect absorbers [11, 12]. Among them, the meta-holograms play a pivotal role in optical imaging fields due to their striking properties including low loss, high resolution, and ease of fabrication.

Various advancements in metasurface-based holograms have been demonstrated over the past few decades, including multicolor holograms [13–15], 2D and three-dimensional (3D) holograms [16–20], full-space holograms [21, 22], space-asymmetric propagation holograms [23–25], and reconfigurable holograms [26–30]. Despite these achievements, there remains a pressing demand for new functionalities and enhanced performance. One emerging direction involves the multiplexing of meta-holograms via diverse light-matter interaction mechanisms to expand information capacity and bolster holographic encryption security.

To this end, a variety of multiplexing strategies have been introduced. Polarization multiplexing [31–33], one of the most mature approaches, leverages the anisotropic or chiral response of meta-atoms to generate distinct holographic images under orthogonal linear or circular polarization states. Wavelength multiplexing exploits the dispersion characteristics of meta-atoms to achieve spectral selectivity, thereby enabling the encoding

* Corresponding authors: Liqiao Jing (liqiaoj@zju.edu.cn); Min Li (minli@ahau.edu.cn); Zuojia Wang (zuojiawang@zju.edu.cn).

of separate images at different frequencies [34–37]. Spatial-frequency multiplexing has also been demonstrated by allocating multiple images into non-overlapping spatial frequency domains [38], which facilitates computational separation and reconstruction through Fourier-domain filters without the need for additional physical layers. More recently, orbital angular momentum multiplexing [39–42] has emerged as a powerful high-dimensional approach, wherein holographic channels are encoded into light beams carrying distinct topological charges, thereby significantly expanding the available channel space by exploiting orthogonal spatial modes. Furthermore, active or reconfigurable metasurfaces incorporating phase-change materials, liquid crystals, or mechanical actuation have been employed to dynamically switch between holographic images in real time [43–48]. Despite these advancements, further enhancement of holographic channel capacity without sacrificing compactness or system complexity remains an open and critical challenge.

Among the various degrees of freedom available in metasurface-based holograms, the incident illumination angle remains a promising yet not fully explored parameter. Angle-multiplexed metasurfaces, which exploit variations in the angle of incidence to encode independent image channels, offer a promising avenue for enhancing channel capacity. Conventional strategies typically employ locally angle-sensitive meta-atoms engineered to yield different phase profiles under varying incidence angles [49–53]. However, the number of independent channels is inherently constrained by the local response characteristics and fabrication constraints. Moreover, it is very necessary to understand the intricate light-matter interaction in the design process of those meta-particles, which is conventionally investigated case-by-case through time-consuming numerical full-wave simulation until a locally optimized solution appears.

In this paper, we present a globally systematic design framework for angle-multiplexed metasurface holography by employing diffractive neural networks. In contrast to conventional approaches that depend on locally optimized meta-atom responses, our method exploits the globally coherent superposition of the entire metasurface aperture to encode multiple holographic channels within a single-layer structure. By incorporating complex electric field distributions under varying illumination angles and their corresponding target images into a unified training dataset, the DNN learns an optimal phase profile that enables angle-dependent wavefront reconstruction. Full 2π phase modulation is achieved via the geometric phase mechanism under circularly polarized illumination. As a proof of concept, a meta-hologram that reconstructs two high-fidelity holographic images under two distinct oblique illuminations is experimentally demonstrated. The proposed method offers new paradigms for wavefront engineering in angle multiplexing, with the potential applications in 3D display, augmented reality, and secure optical communication systems.

2. RESULTS

The schematic illustration of the functionality and working principle of the proposed angle-multiplexed metasurface are shown in Fig. 1. Analogous to the artificial neural network, a DNN in the optical domain, which consists of an input layer, a hidden layer, and an output layer, enables efficient wavefront manipulation and ultrafast information processing through light propagation. From a machine learning perspective, the mapping between incident angles and their corresponding holographic images can be viewed as a classification task, where each illumination angle represents a distinct input category. The input layer corresponds to the complex electric field distribution of the incident wave, while the output layer represents the amplitude profile of the reconstructed hologram.

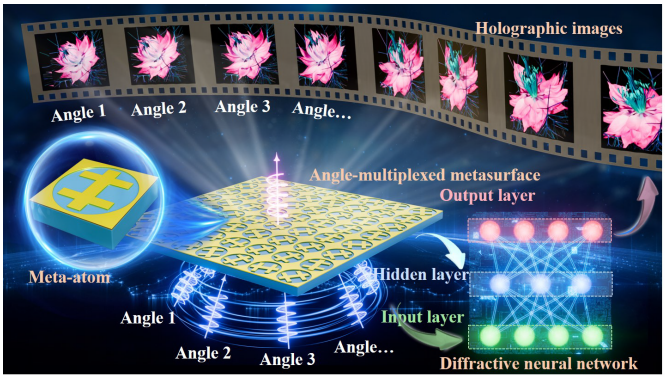

FIGURE 1. Schematic illustration of the proposed angle-multiplexed metasurface and its working principle. The angle-multiplexed metasurface functions as an optical-domain deep neural network, consisting of an input layer (incident wave), a hidden layer (metasurface), and an output layer (reconstructed hologram). Each incident angle is treated as a distinct input category, enabling the effective generation of holographic images under different illumination angles.

2.1. Design Principle of the DNN-Based Angle-Multiplexed Metasurface

The metasurface, functioning as the hidden layer, is composed of a dense array of subwavelength meta-atoms that decode the angle-dependent encoded input and generate the desired output field. According to the Huygens principle, each point on a propagating wavefront acts as a secondary source of spherical wavelets, so each meta-atom behaves as an individual neuron in the neural network, modulating the phase of the incoming wave and interconnecting with elements in the following layer through free-space diffraction. Adhering to the Rayleigh-Sommerfeld diffraction equation, the field located at an arbitrary position $\vec{r}^{\,l+1} = (x^{l+1}, y^{l+1}, z^{l+1})$ in a subsequent layer is determined by the collective contribution of all meta-atoms in the preceding layer, which is expressed as follows:

$$E\left(\vec{r}^{\,l+1}\right) = \iint_{-\infty}^{\infty} \frac{z - z_i}{2\pi R^2}\left(\frac{1}{R} - jk\right) e^{jkR} \cdot E\left(\vec{r}_i^{\,l}\right) \cdot t\left(\vec{r}_i^{\,l}\right) dxdy \tag{1}$$

Here, l represents the lth layer in the DNN; $\vec{r}_i^{\,l} = (x_i^l, y_i^l, z_i^l)$ refers the position of the ith meta-atom in layer l; λ is the wavelength of the incident wave in vacuum; and $R = ((x^{l+1} - x_i^l)^2 + (y^{l+1} - y_i^l)^2 + (z^{l+1} - z_i^l)^2)^{1/2}$ denotes the distance

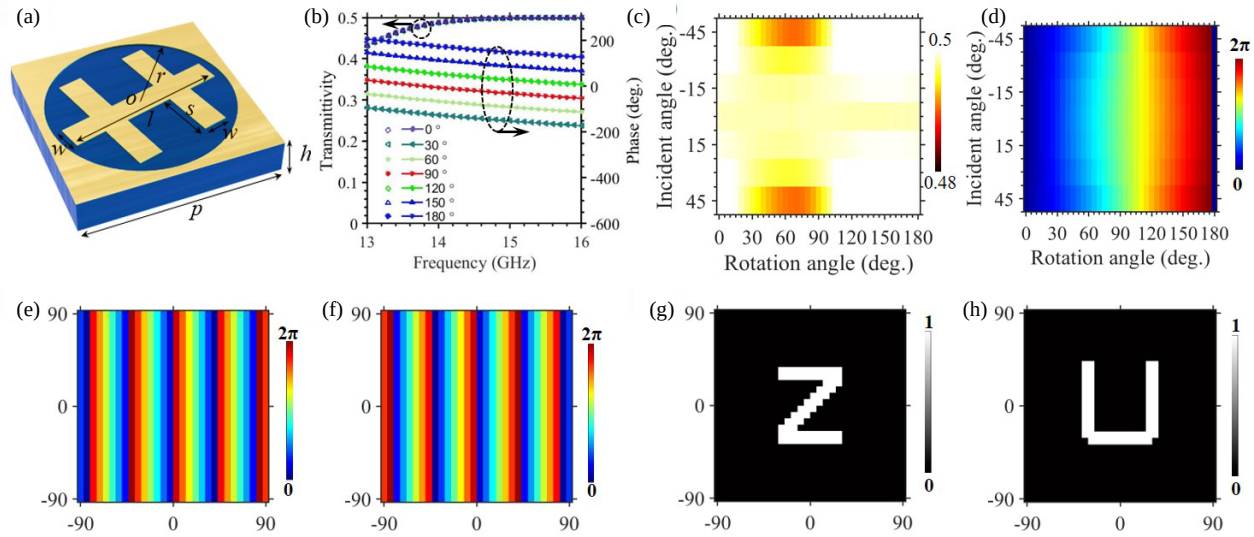

FIGURE 2. (a) Geometric configuration of the meta-atom. (b) Simulated amplitude and phase responses of the cross-polarized transmission coefficient T_{-+} as functions of the rotation angle φ under normal incidence. (c) Amplitude and (d) phase responses of T_{-+} as functions of rotation angle and incident angles at 15 GHz. Phase distributions under (e) $-30°$ incidence and (f) $30°$ incidence, respectively. Target holographic images under (g) $-30°$ incidence and (h) $30°$ incidence, respectively.

between two meta-atoms. The complex transmission coefficient of each meta-atom is denoted by $t(\vec{r}_i^{\,l}) = a_i^l(x_i^l, y_i^l, z_i^l) \cdot \exp(j\phi_i^l(x_i^l, y_i^l, z_i^l))$, where $a_i^l(x_i^l, y_i^l, z_i^l)$ and $\phi_i^l(x_i^l, y_i^l, z_i^l)$ represent the amplitude and phase terms, respectively. Considering the high transmission efficiency of the meta-atom, the amplitude term $a_i^l(x_i^l, y_i^l, z_i^l)$ is treated as a constant for simplification. Assuming that the DNN consists of M hidden layers, the energy intensity at the output plane is $s_k^{M+1} = |E_k^{M+1}|^2$, and the loss function is defined as a mean squared error of the target field g_k^{M+1} and the actual predicted field s_k^{M+1}:

$$f\left(\phi_i^l\right) = \frac{1}{K}\sum\nolimits_k \left(s_k^{M+1} - g_k^{M+1}\right)^2 \tag{2}$$

where K denotes the total number of sample points across the output plane. The design objective is to minimize the predefined loss function that quantifies the discrepancy between the reconstructed and target holographic images, under multiple incident angles. This minimization is performed using a gradient-based backpropagation algorithm. In the DNN, the trainable weights are physically realized by the phase responses of the individual meta-atoms on the metasurface. As a result, the inverse design problem is formulated such that the phase profiles of the meta-atoms are iteratively updated, enabling the metasurface to simultaneously reconstruct all target holographic images. The general form of this optimization problem is outlined as follows:

$$\min_{\phi_i^l} f\left(\phi_i^l\right), \quad s.t.\ 0 \le \phi_i^l \le 2\pi \tag{3}$$

2.2. Design of the Meta-Atom

To enable precise control over the electromagnetic wavefront under circularly polarized illumination, the meta-atom is designed based on the geometric phase mechanism, as illustrated in Fig. 2(a). The structural configuration consists of two vertically oriented metallic bars and one horizontally aligned bar, all encapsulated within a copper frame to effectively suppress near-field coupling between adjacent elements. Electromagnetic response characterization of the meta-atom is performed using full-wave simulations in CST Microwave Studio, with unit-cell boundary conditions applied along the lateral directions and Floquet ports defined along the z-direction. The geometric parameters are optimized as follows: $l = 3.9\,\text{mm}$, $w = 0.75\,\text{mm}$, $s = 1.575\,\text{mm}$, and $p = 6\,\text{mm}$. The relative dielectric constant, loss tangent, and thickness of the bottom F4B dielectric substrate are $\varepsilon_r = 3$, $\tan\delta = 0.002$, and $h = 0.25\,\text{mm}$, respectively.

The cross-polarized transmission coefficient T_{-+} as a function of the rotation angle φ under normal incidence of right-handed circularly polarized (RHCP) waves is illustrated in Fig. 2(b). By varying the in-plane rotation angle φ from $0°$ to $180°$, the transmitted phase achieves continuous modulation over a full 2π range. Simultaneously, the transmission amplitude remains above 0.49 within the 14–16 GHz band, approaching the theoretical limit of the cross-polarized transmission coefficient of 0.5 for the single-layer metasurface structure. In view of the dual-channel holographic imaging enabled by angle multiplexing, the angular robustness of the designed meta-atom is further investigated under distinct oblique incidences. As shown in Fig. 2(c), the cross-polarized transmission amplitude remains stable between 0.48 and 0.5 as the incident angle sweeps from $-45°$ to $45°$ at the operating frequency of 15 GHz. Fig. 2(d) further confirms that the transmission phase exhibits negligible variation with respect to changes in the incidence angle, indicating excellent angular stability of the meta-atom design.

2.3. Training Strategy for the DNN

As a conceptual demonstration, we first present a dual-channel holographic imaging task involving two distinct illumination angles. Specifically, the metasurface reconstructs the letter "Z"

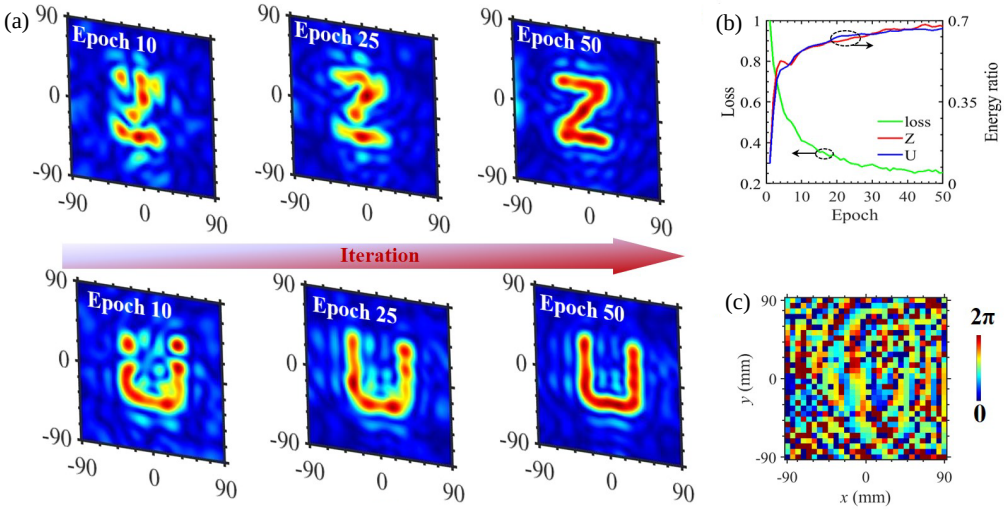

FIGURE 3. Training process and optimization results by a DNN. (a) Evolution of the reconstructed holographic images under illumination angles of -30° and 30° across representative training epochs (10, 25, and 50). (b) Energy ratio for each target hologram and the total loss value versus training epoch. (c) Optimized phase profile after convergence of the training process.

at the imaging plane under -30° illumination, whereas under $+30^\circ$ incidence, the letter "U" is reconstructed. When a plane wave is characterized by an incident angle $\theta = (\theta_x, \theta_y)$ and a wavelength λ impinges upon the metasurface, the resulting complex amplitude distribution on the substrate, specifically at the plane $z = 0$, can be rigorously described by

$$U(x, y) = U_0 \exp(jk_x x + jk_y y) \tag{4}$$

where $k_x = k_0 \sin\theta_x$, $k_y = k_0 \sin\theta_y$, and $k_0 = 2\pi/\lambda$. Under the specific illumination condition where incidence is along the x-axis, the resulting complex field at the substrate interface ($z = 0$) can be expressed in a simplified form $U(x, y) = U_0 \exp(jk_x x)$. A relative phase delay $\Delta\varphi = k_x \Delta x$ arises due to the lateral displacement Δx between adjacent elements. The phase distributions of the incident waves under -30° and $+30^\circ$ illuminations, serving as the input layer of the DNN, are illustrated in Figs. 2(e) and 2(f), respectively. The corresponding target holographic patterns at the output layer are shown in Figs. 2(g) and 2(h), respectively.

The metasurface, serving as the hidden layer in DNN, consists of 30×30 meta-atoms over an area of $180 \times 180\,\text{mm}^2$. During training, both the incident phase profiles and target field distributions are discretized into 30×30 matrices and input into the network. The training process is iterated 50 epochs. Representative predicted holographic images at epochs 10, 25, and 50 are illustrated in Fig. 3(a), showing the progressive refinement of image quality during training. The corresponding energy ratios for each target image, along with the total loss value across epochs, are presented in Fig. 3(b). By the 10th iteration, the basic target contour emerges, albeit with noticeable discontinuities and significant background noise. At this stage, the error metric decreases sharply from 1.0 to approximately 0.4. The energy ratios for the reconstructed "Z" and "U" images reach 56.9% and 56.8%, respectively. After 25 iterations, the error further decreases to 0.3, and the energy ratios increase to 62.7% and 63.7%, yielding sharper image boundaries though still affected by residual noise. Following 50 training iterations, the network output converges with a final error of 0.25, and the energy ratios of the "Z" and "U" images reach 67.7% and 66.6%, respectively. The resulting holographic images exhibit well-defined contours, high contrast, and significantly suppressed background noise. The optimized phase profile of the metasurface after convergence is shown in Fig. 3(c).

2.4. Robustness Analysis of the DNN-Based Metasurface

To evaluate the robustness of the DNN-based metasurface under realistic illumination conditions, we consider the practical scenario where plane wave excitation is typically approximated either by placing the sample in the far field of a feed source or by using a lens to collimate spherical wavefronts. In such cases, the incident field generally exhibits amplitude non-uniformity. To evaluate the impact of this non-ideal illumination, the additive white Gaussian noise with a signal-to-noise ratio (SNR) of 3 dB is introduced to the amplitude of the incident wave, as shown in Fig. 4(a). The reconstructed images under -30° and $+30^\circ$ incidence are presented in Fig. 4(b) and Fig. 4(d), respectively. Despite the presence of noise, both reconstructed images retain high visual fidelity, although certain regions exhibit slight amplitude inhomogeneities. The corresponding relative error maps are shown in Fig. 4(c) and Fig. 4(e), with average relative errors of 10.3% for the "Z" image and 11.3% for the "U" image. When the SNR is increased to 5 dB (Fig. 4(f)), the reconstructed images (Fig. 4(g) and Fig. 4(i)) become even clearer, with more uniform amplitude distributions. As shown in the corresponding relative error maps (Fig. 4(h) and Fig. 4(j)), the average relative error is 6.9% for the "Z" image and 6.3% for the "U" image, respectively.

To further examine the robustness of the DNN-based metasurface, we next evaluate the impact of phase errors, which are inevitable in practical implementations due to fabrication tolerances or imperfect phase modulation. Based on the optimized phase profile, we introduce a uniformly distributed random

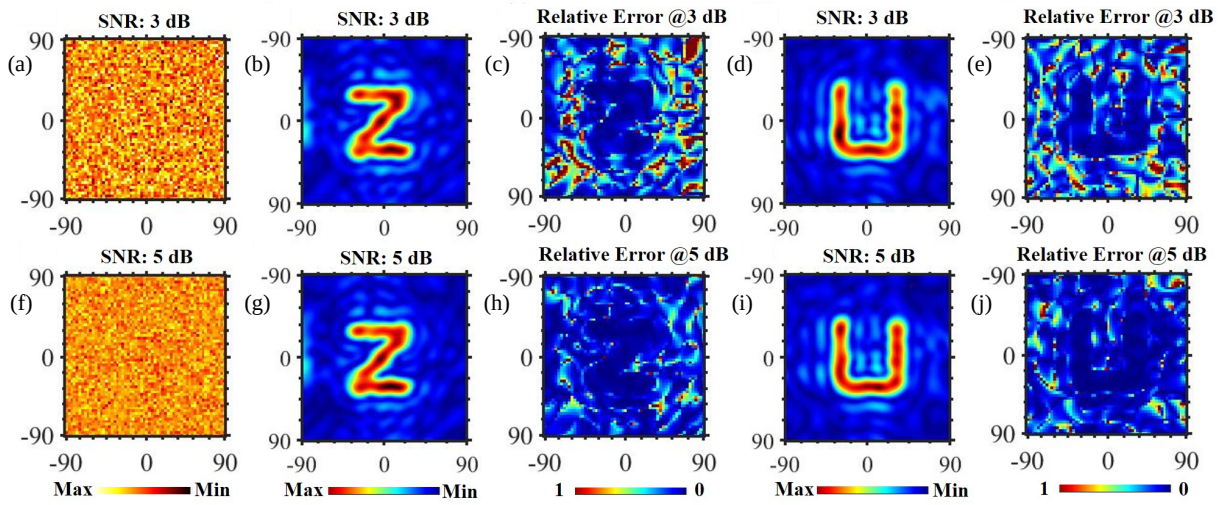

FIGURE 4. Robustness analysis of the DNN-based metasurface under non-ideal illumination conditions. (a) Non-uniform illumination is achieved by introducing additive white Gaussian noise with an SNR of 3 dB to the incident wave amplitude. (b) Reconstructed holographic image and (c) corresponding relative error map under $-30°$ incidence with an SNR of 3 dB. (d) Reconstructed holographic image and (e) corresponding relative error map under $30°$ incidence with an SNR of 3 dB. (f) Non-uniform illumination is achieved by introducing additive white Gaussian noise with an SNR of 5 dB to the incident wave amplitude. (g) Reconstructed holographic image and (h) corresponding relative error map under $-30°$ incidence with an SNR of 5 dB. (i) Reconstructed holographic image and (j) corresponding relative error map under $30°$ incidence with an SNR of 5 dB.

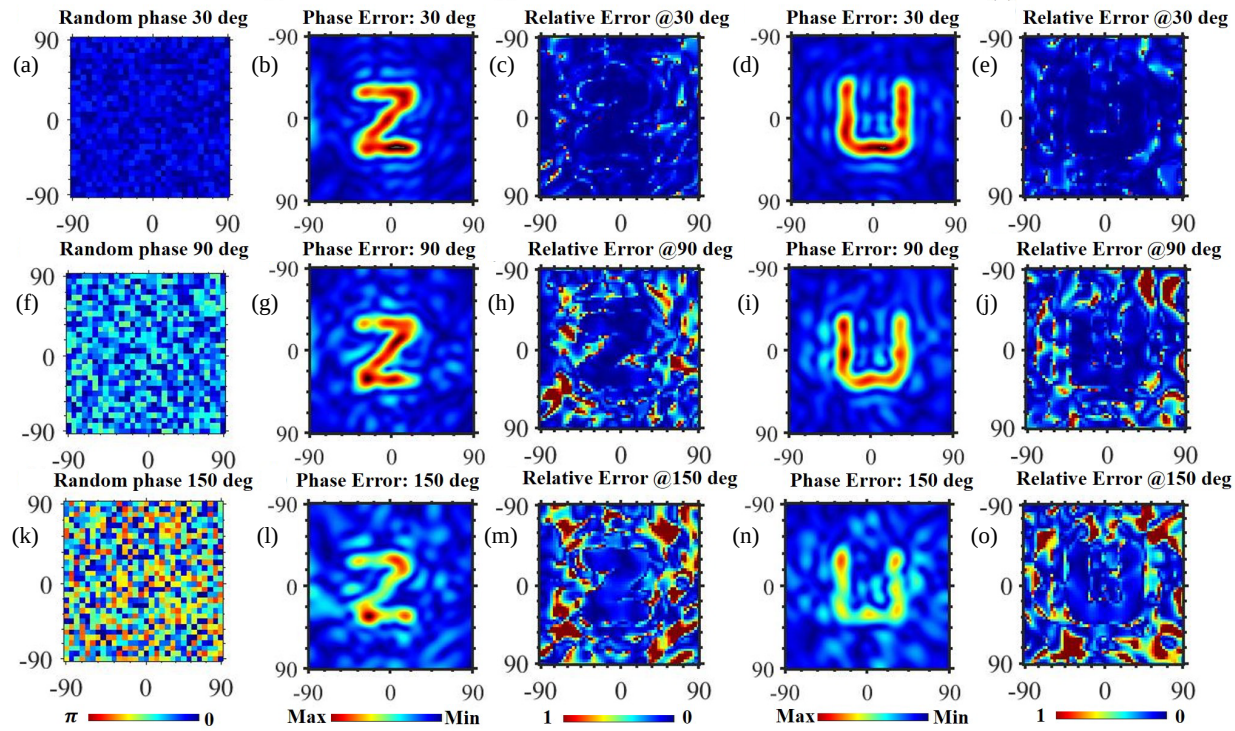

FIGURE 5. Robustness analysis of the DNN-based metasurface under random phase perturbations. (a) Phase error is introduced by adding uniformly distributed random phase noise within the range of $0°$–$30°$ to the optimized phase profile. (b) Reconstructed holographic image and (c) corresponding relative error map under $-30°$ incidence with phase perturbations within the range of $0°$–$30°$. (d) Reconstructed holographic image and (e) corresponding relative error map under $30°$ incidence with phase perturbations within the range of $0°$–$30°$. (f) Phase error within the range of $0°$–$90°$. (g) Reconstructed holographic image and (h) corresponding relative error map under $-30°$ incidence with phase perturbations within the range of $0°$–$90°$. (i) Reconstructed holographic image and (j) corresponding relative error map under $30°$ incidence with phase perturbations within the range of $0°$–$90°$. (k) Phase error within the range of $0°$–$150°$. (l) Reconstructed holographic image and (m) corresponding relative error map under $-30°$ incidence with phase perturbations within the range of $0°$–$150°$. (n) Reconstructed holographic image and (o) corresponding relative error map under $30°$ incidence with phase perturbations within the range of $0°$–$150°$.

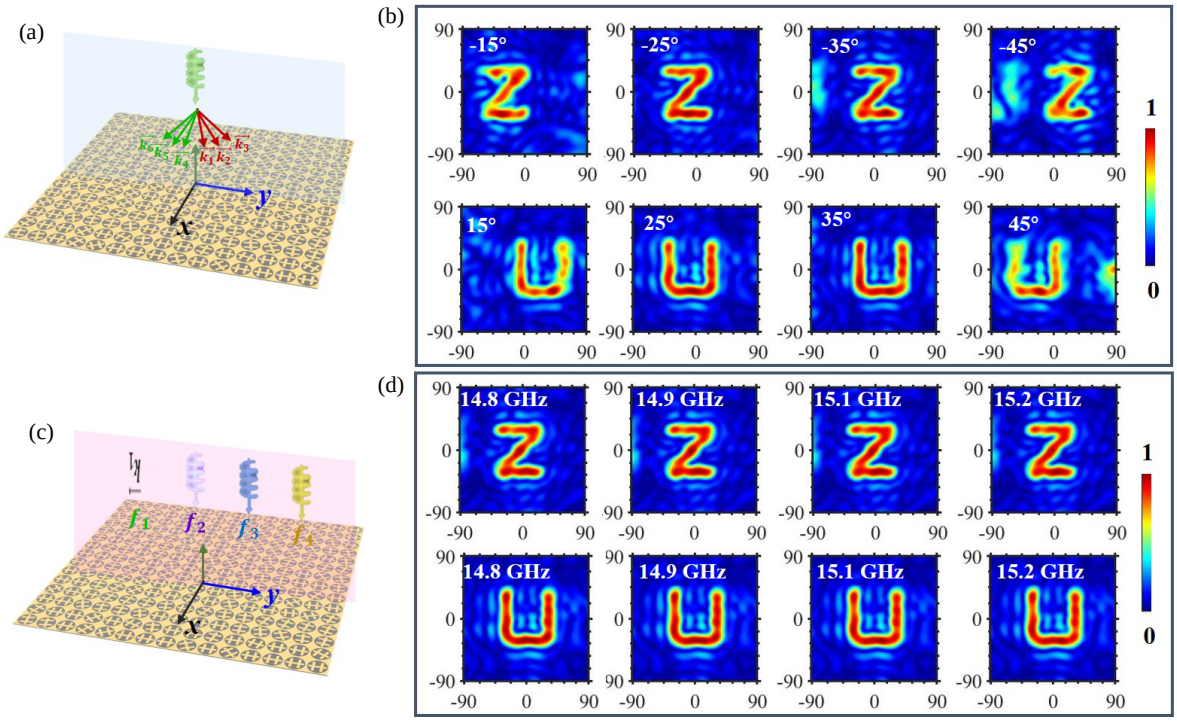

FIGURE 6. Robustness of the angle-multiplexed metasurface against variations in incident angle and operating frequency. (a) Schematic diagram of different incident angles. (b) Reconstructed electric field distributions under varying illumination angles from $-15°$ to $+45°$ at 15 GHz. (c) Schematic diagram of different incident frequencies. (d) Reconstructed electric field distributions under varying illumination frequencies from 14.8 GHz to 15.2 GHz.

phase perturbation within the range of $0°$ to $30°$, as illustrated in Fig. 5(a). The reconstructed images under $-30°$ and $+30°$ incidence are presented in Fig. 5(b) and Fig. 5(d), respectively. While the overall image structures remain discernible, certain regions exhibit slight amplitude non-uniformity due to the imposed phase noise. The corresponding relative error maps are shown in Fig. 5(c) and Fig. 5(e), with average relative errors of 12.1% for the "Z" image and 10.3% for the "U" image. When the random phase error is increased to the range of $0°$ to $90°$, as shown in Fig. 5(f), the reconstructed images (Fig. 5(g) and Fig. 5(i)) begin to degrade, with noticeable blurring and reduced image quality. The corresponding error maps (Fig. 5(h) and Fig. 5(j)) indicate average relative errors of 31.1% for the "Z" image and 28.0% for the "U" image. As the phase perturbation range further increases to $0°$–$150°$ (Fig. 5(k)), the image quality deteriorates significantly, as shown in the reconstructions in Fig. 5(l) and Fig. 5(n). Severe distortions such as discontinuities and increased background noise are observed. The associated relative error maps (Fig. 5(m) and Fig. 5(o)) reveal average relative errors of 55.6% and 48.3% for the "Z" and "U" images, respectively.

The designed angle-multiplexed metasurface also exhibits strong robustness against variations in both incident angle (as shown in Fig. 6(a)) and operating frequency (as shown in Fig. 6(c)). Fig. 6(b) presents the reconstructed electric field distributions for incident angles ranging from $-15°$ to $-45°$ and from $+15°$ to $+45°$. The results indicate that small angular deviations, such as a $5°$ offset from the design angle, have minimal influence on image clarity. Although slight positional shifts in the reconstructed images can be observed, the image contours remain well preserved. As the incident angle increases to $15°$, image quality gradually deteriorates, manifested by reduced sharpness, elevated background noise, and a more pronounced displacement in image position. The angular robustness stems from the diffractive nature of the metasurface holography, which inherently tolerates small deviations in the incident angle. Furthermore, the smoothly varying phase profile across the aperture reduces sensitivity to oblique incidence variations. As illustrated in Fig. 6(d), when the operating frequency deviates by up to ± 0.2 GHz from the design frequency, the images remain well defined, indicating that the learned phase profile retains functionality over a reasonable bandwidth. The frequency robustness stems from the broadband response of the meta-atoms, which are capable of maintaining the designed phase modulation across a relatively wide frequency range. The frequency robustness is attributed to the broadband behavior of the meta-atoms, which preserve their intended phase response over a wide range of operating frequencies. This stability arises from the non-resonant nature of the geometric phase mechanism, allowing consistent phase modulation without strong frequency dependence.

2.5. Evaluation of Angular Multiplexing Capacity

Besides, to further qualitatively evaluate the theoretical limit of angular multiplexing capacity, we numerically investigate the relationship between image fidelity and the number of incident

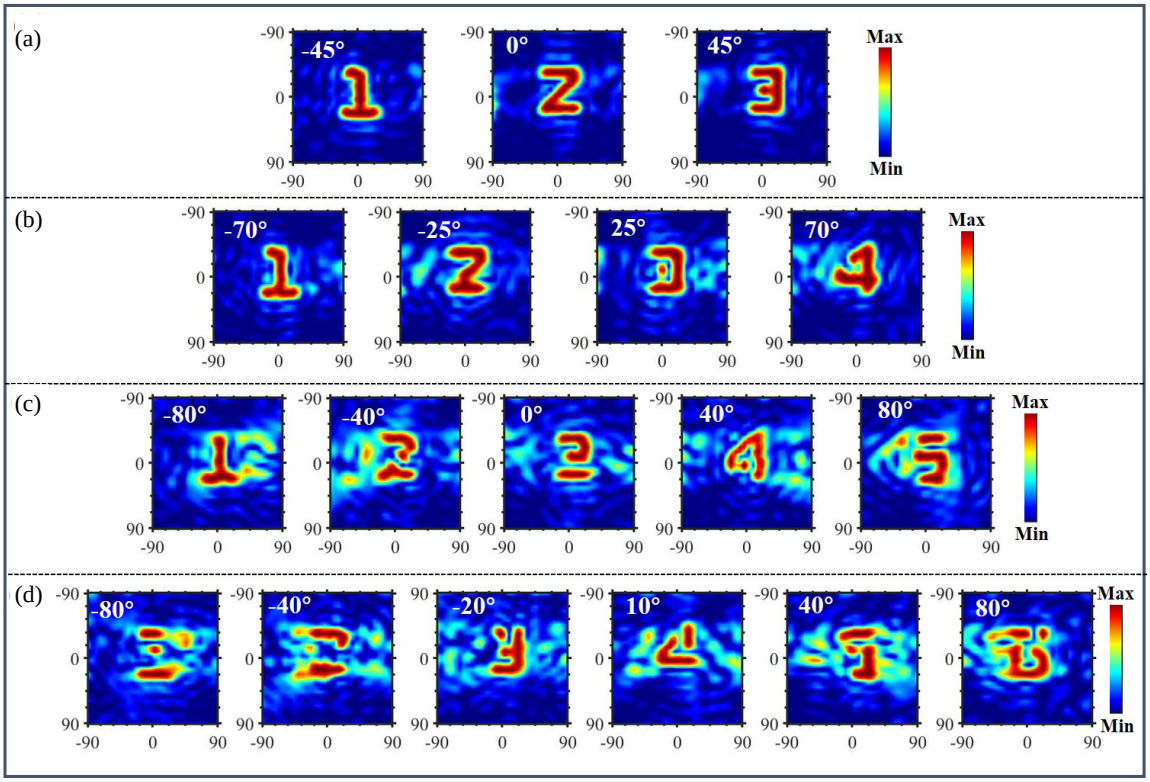

FIGURE 7. Reconstructed images under increasing numbers of multiplexed incident angles. (a) Three incident angles $-45°$, $0°$, and $45°$. (b) Four incident angles $-70°$, $-25°$, $25°$, and $70°$. (c) Five incident angles $-80°$, $-40°$, $0°$, $40°$, and $80°$. (d) Six incident angles $-80°$, $-40°$, $-20°$, $10°$, $40°$, and $80°$.

angles. Under the assumption that the meta-atoms exhibit no angular dispersion, as shown in Fig. 7(a), with three incident angles ($-45°$, $0°$, and $45°$), the reconstructed digits "1", "2", and "3" are sharp and exhibit uniform intensity. With four angles ($-70°$, $-25°$, $25°$, and $70°$), the digits "1" to "4" remain distinguishable as presented in Fig. 7(b), though minor discontinuities begin to appear, particularly in the representations of "3" and "4". As the number increases to five ($-80°$, $-40°$, $0°$, $40°$, and $80°$), it can be observed in Fig. 7(c) that only coarse outlines of digits "1" to "5" are visible, with notable degradation in completeness and the emergence of background noise. As shown in Fig. 7(d), when the number further increases to six ($-80°$, $-40°$, $-20°$, $10°$, $40°$, and $80°$), the reconstructed images become severely degraded, and the digits are no longer visually recognizable. These results demonstrate a clear trade-off between the angular channel capacity and the quality of reconstructed images, where inter-angle interference and limited angular resolution collectively constrain the maximum achievable number of high-quality multiplexed channels.

2.6. Simulation and Experimental Validation

Full-wave electromagnetic simulations are conducted using CST Microwave Studio 2019 to verify the performance of the designed metasurface under realistic conditions. The 3D simulation model, along with precise structural parameters, is presented in Fig. 8(a). In the simulation setup, Perfectly Matched Layer (PML) boundary conditions are applied along the transverse x- and y-directions to eliminate artificial reflections, while the longitudinal z direction is terminated with open (add space) boundary conditions to mimic propagation into free space. An RHCP plane wave is employed as the incident excitation. On the observation plane located 90 mm away from the metasurface, the normalized electric field intensity distributions corresponding to incident angles $-30°$ and $+30°$ are presented in Figs. 8(b) and 8(c), respectively, over a frequency span from 14.8 GHz to 15.2 GHz. At the design frequency of 15 GHz, the reconstructed field profiles exhibit well-defined and high-contrast images that closely resemble the intended target patterns "Z" and "U". Within a ± 0.2 GHz deviation from the central frequency, the image quality remains largely preserved, maintaining clear contours and structural integrity.

A near-field scanning system, as illustrated in Fig. 9(a), is constructed to experimentally characterize the electric field intensity distributions. Since the tangential component of the electric field contains both x and y polarizations, two orthogonally polarized probes are employed to separately acquire the field components across the scanning plane. The total amplitude of the tangential electric field is then calculated by $|E_t| = \sqrt{|E_x|^2 + |E_y|^2}$. When an RHCP plane wave is incident on the metasurface at an angle of $-30°$, the recorded field intensity at a distance of 90 mm from the metasurface aperture reveals a clearly defined "Z"-shaped pattern as illustrated in Fig. 9(b). Similarly, for a $+30°$ incident angle, a distinct "U"-shaped intensity profile is observed in Fig. 9(c). These experimentally measured results exhibit strong agreement with both theoreti-

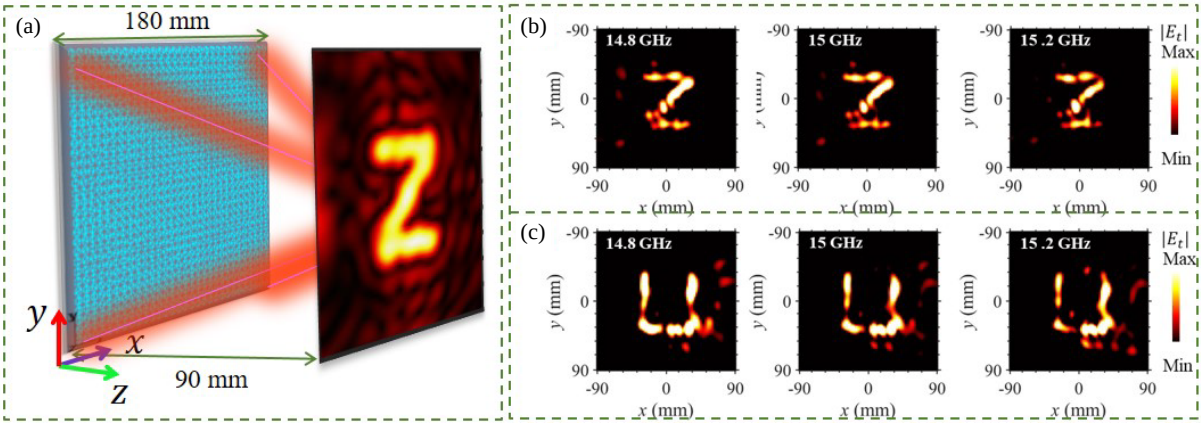

FIGURE 8. Full-wave simulation results. (a) Model illustration in CST. Simulated normalized electric field intensity on the imaging plane with frequency increasing from 14.8 GHz to 15.2 GHz under (b) -30° incidence and (c) 30° incidence, respectively.

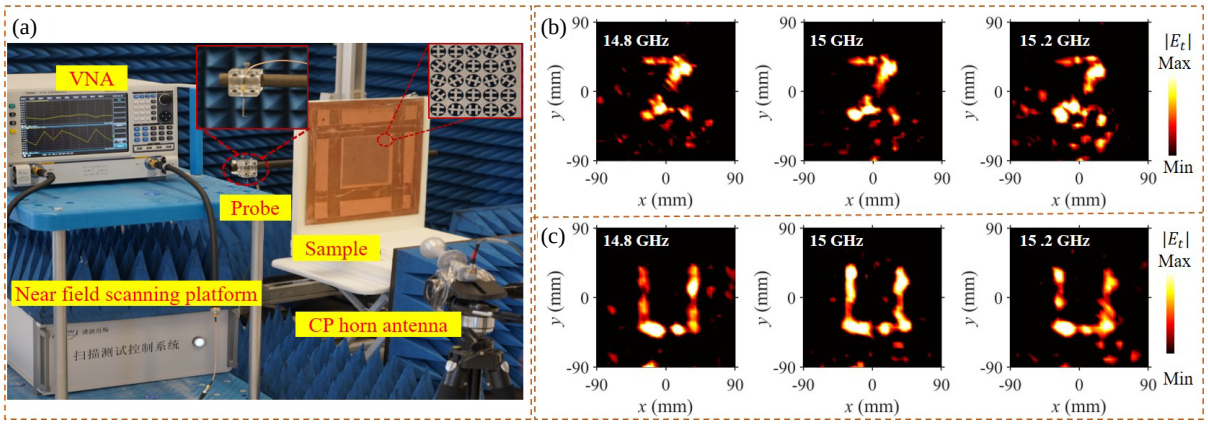

FIGURE 9. Experiment results. (a) Measurement setup. Measured imaging performance at $z = 90$ mm for different frequencies from 14.8 GHz to 15.2 GHz under (b) -30° incidence and (c) 30° incidence, respectively.

cal calculations and full-wave simulations, thereby confirming that the proposed metasurface design enables independent and precise near-field amplitude modulation for obliquely incident circularly polarized waves.

3. METHODS

Simulation. Full-wave simulations are conducted using CST Microwave Studio 2019. The transmission amplitudes and phases of the proposed single-layer transmission-type meta-atoms are simulated with periodic boundary conditions. A three-dimensional model of the angle-multiplexed metasurface hologram, composed of 30×30 meta-atoms within a $180 \times 180\,\text{mm}^2$ aperture, is constructed. To replicate free space conditions, PML boundary conditions are applied along the x- and y-directions, and open (add space) boundary conditions are used in the z-direction. A right-handed circularly polarized plane wave is used as the excitation source, incident at designated oblique angles. The complex electric field distribution is monitored on an observation plane positioned 90 mm behind the metasurface. Simulations are performed at multiple frequencies ranging from 14.8 GHz to 15.2 GHz.

Experimental setup. In the near-field measurement, a right-handed circularly polarized horn antenna is connected to port 1 of the vector network analyzer (ZVA67) and positioned $30\lambda_0$ away from the metasurface sample to generate quasi-plane wave illumination. The sample is fixed on a stable platform, and the incident angle is adjusted by rotating the sample holder accordingly. An electric field probe connected to port 2 of the VNA is mounted on a computer-controlled motorized scanning stage. The probe is sequentially oriented along the x- and y-directions to measure the corresponding components of the electric field. During scanning, the probe moves across a planar region measuring $180 \times 180\,\text{mm}^2$, located 90 mm behind the metasurface. Field data acquisition is performed point by point across the defined scan area. The scanning system is synchronized with the VNA through the control software to ensure accurate spatial sampling and data recording at each position.

4. CONCLUSION

In summary, we have demonstrated a DNN-enabled design strategy for angle-multiplexed metasurface holography that overcomes the inherent limitations imposed by the angular

optical memory effect. By replacing traditional local meta-atom optimization with a global training framework, the proposed method enables the independent reconstruction of multiple holographic images under distinct oblique illuminations using a single-layer metasurface. The integration of complex electric field distributions and corresponding target images into the training process allows the neural network to learn an optimal phase profile that governs the angular selectivity of the output wavefronts. The geometric phase for circularly polarized light is used to ensure broadband, full-phase modulation while maintaining structural simplicity and fabrication feasibility. Experimental validations confirm that the designed metasurface achieves high-fidelity image reconstruction under both incidence angles, in strong agreement with numerical simulations. The proposed metasurface, along with its design strategy, offers a fresh perspective for crafting multiplexing holograms and holds promise for diverse applications, including multifunctional devices and reconfigurable imaging systems. Furthermore, the DNN-like design strategy can be extended to acoustics and optics, readily adaptable to the design of meta-devices with multiple layers, providing considerable freedom to achieve multifunctional reconfigurability.

ACKNOWLEDGEMENT

The work was sponsored by the National Natural Science Foundation of China (NNSFC) (62222115, 62171407, 62401015, 62201500), the Key Research and Development Program of Zhejiang Province (2024C01241(SD2)), the Natural Science Foundation of Zhejiang Province (ZCLY24F0101), the Natural Science Foundation of Anhui Province (2408085QF182) and the Fundamental Research Funds for the Central Universities.

REFERENCES

[1] Qian, C., B. Zheng, Y. Shen, L. Jing, E. Li, L. Shen, and H. Chen, "Deep-learning-enabled self-adaptive microwave cloak without human intervention," *Nature Photonics*, Vol. 14, No. 6, 383–390, 2020.

[2] Chen, H., B.-I. Wu, B. Zhang, and J. A. Kong, "Electromagnetic wave interactions with a metamaterial cloak," *Physical Review Letters*, Vol. 99, No. 6, 063903, 2007.

[3] Chen, H., B. Zheng, L. Shen, H. Wang, X. Zhang, N. I. Zheludev, and B. Zhang, "Ray-optics cloaking devices for large objects in incoherent natural light," *Nature Communications*, Vol. 4, No. 1, 2652, 2013.

[4] Wang, S., Z.-L. Deng, Y. Wang, Q. Zhou, X. Wang, Y. Cao, B.-O. Guan, S. Xiao, and X. Li, "Arbitrary polarization conversion dichroism metasurfaces for all-in-one full Poincaré sphere polarizers," *Light: Science & Applications*, Vol. 10, No. 1, 24, 2021.

[5] Yu, S., L. Li, G. Shi, C. Zhu, and Y. Shi, "Generating multiple orbital angular momentum vortex beams using a metasurface in radio frequency domain," *Applied Physics Letters*, Vol. 108, No. 24, 241901, 2016.

[6] Liao, D., X. Ren, L. Jing, M. Li, H. Chen, and Z. Wang, "Chiral metasurface enabled circularly polarized OAM-generating folded transmitarray antenna with high-gain low-profile and broadband characteristics," *IEEE Transactions on Antennas and Propagation*, Vol. 71, No. 6, 4737–4746, 2023.

[7] Ni, X., A. V. Kildishev, and V. M. Shalaev, "Metasurface holograms for visible light," *Nature Communications*, Vol. 4, No. 1, 2807, 2013.

[8] Li, L., T. J. Cui, W. Ji, S. Liu, J. Ding, X. Wan, Y. B. Li, M. Jiang, C.-W. Qiu, and S. Zhang, "Electromagnetic reprogrammable coding-metasurface holograms," *Nature Communications*, Vol. 8, No. 1, 197, 2017.

[9] Chen, M. K., Y. Wu, L. Feng, Q. Fan, M. Lu, T. Xu, and D. P. Tsai, "Principles, functions, and applications of optical meta-lens," *Advanced Optical Materials*, Vol. 9, No. 4, 2001414, 2021.

[10] Wang, Z., L. Song, X. Zhang, X. Wang, Z. Wang, H. Chen, M. Li, and D. Liao, "Synergizing radiation regulation and cross-band stealth with passive folded metasurfaces," *Advanced Functional Materials*, Vol. 35, No. 28, 2421782, 2025.

[11] Wang, Z., H. Jia, K. Yao, W. Cai, H. Chen, and Y. Liu, "Circular dichroism metamirrors with near-perfect extinction," *ACS Photonics*, Vol. 3, No. 11, 2096–2101, 2016.

[12] Liang, Y., H. Lin, K. Koshelev, F. Zhang, Y. Yang, J. Wu, Y. Kivshar, and B. Jia, "Full-stokes polarization perfect absorption with diatomic metasurfaces," *Nano Letters*, Vol. 21, No. 2, 1090–1095, 2021.

[13] Wang, B., F. Dong, Q.-T. Li, D. Yang, C. Sun, J. Chen, Z. Song, L. Xu, W. Chu, Y.-F. Xiao, *et al.*, "Visible-frequency dielectric metasurfaces for multiwavelength achromatic and highly dispersive holograms," *Nano Letters*, Vol. 16, No. 8, 5235–5240, 2016.

[14] Li, X., L. Chen, Y. Li, X. Zhang, M. Pu, Z. Zhao, X. Ma, Y. Wang, M. Hong, and X. Luo, "Multicolor 3D meta-holography by broadband plasmonic modulation," *Science Advances*, Vol. 2, No. 11, e1601102, 2016.

[15] Zheng, Y.-W., F. Chu, F.-C. Lin, Y.-X. Hu, Y.-L. Li, Y. Zheng, D. Wang, and Q.-H. Wang, "Wide-viewing-angle color holographic 3D display system with high brightness encoding," *PhotoniX*, Vol. 6, No. 1, 3, 2025.

[16] Sun, S., J. Li, X. Li, Y. Feng, and L. Chen, "Ferrofluid-assisted dynamic metasurface 3D holography endowed with rapid, linear, and high-contrast color modulation," *Laser & Photonics Reviews*, Vol. 19, No. 8, 2401417, 2025.

[17] Li, J., X. Li, X. Huang, R. Kaissner, F. Neubrech, S. Sun, and N. Liu, "High space-bandwidth-product (SBP) hologram carriers toward photorealistic 3D holography," *Laser & Photonics Reviews*, Vol. 18, No. 7, 2301173, 2024.

[18] Sun, S., J. Li, X. Li, X. Huang, Y. Zhang, and L. Chen, "High-efficiency, broadband, and low-crosstalk 3D holography by multi-layer holographic-lens integrated metasurface," *APL Photonics*, Vol. 9, No. 8, 2024.

[19] Zhao, R., Q. Wei, Y. Li, X. Li, G. Geng, X. Li, J. Li, Y. Wang, and L. Huang, "Stereo jones matrix holography with longitudinal polarization transformation," *Laser & Photonics Reviews*, Vol. 17, No. 8, 2200982, 2023.

[20] Wang, D., Y.-L. Li, X.-R. Zheng, R.-N. Ji, X. Xie, K. Song, F.-C. Lin, N.-N. Li, Z. Jiang, C. Liu, *et al.*, "Decimeter-depth and polarization addressable color 3D meta-holography," *Nature Communications*, Vol. 15, No. 1, 8242, 2024.

[21] Zheng, G., N. Zhou, L. Deng, G. Li, J. Tao, and Z. Li, "Full-space metasurface holograms in the visible range," *Optics Express*, Vol. 29, No. 2, 2920–2930, 2021.

[22] Huang, L., X. Chen, H. Mühlenbernd, H. Zhang, S. Chen, B. Bai, Q. Tan, G. Jin, K.-W. Cheah, C.-W. Qiu, *et al.*, "Three-dimensional optical holography using a plasmonic metasurface," *Nature Communications*, Vol. 4, No. 1, 2808, 2013.

[23] Liang, X., L. Deng, X. Shan, Z. Li, Z. Zhou, Z. Guan, and G. Zheng, "Asymmetric hologram with a single-size nanostructured metasurface," *Optics Express*, Vol. 29, No. 13, 19 964–

19 974, 2021.

[24] Kim, H., J. Jung, and J. Shin, "Bidirectional vectorial holography using bi-layer metasurfaces and its application to optical encryption," *Advanced Materials*, Vol. 36, No. 44, 2406717, 2024.

[25] Chen, K., G. Ding, G. Hu, Z. Jin, J. Zhao, Y. Feng, T. Jiang, A. Alù, and C.-W. Qiu, "Directional Janus metasurface," *Advanced Materials*, Vol. 32, No. 2, 1906352, 2020.

[26] Zhang, M., M. Pu, F. Zhang, Y. Guo, Q. He, X. Ma, Y. Huang, X. Li, H. Yu, and X. Luo, "Plasmonic metasurfaces for switchable photonic spin-orbit interactions based on phase change materials," *Advanced Science*, Vol. 5, No. 10, 1800835, 2018.

[27] Malek, S. C., H.-S. Ee, and R. Agarwal, "Strain multiplexed metasurface holograms on a stretchable substrate," *Nano Letters*, Vol. 17, No. 6, 3641–3645, 2017.

[28] Zhang, X., Y. Gao, W. Hu, Q. Luo, T. Hong, K.-D. Xu, and W. Jiang, "Conformal reconfigurable holographic metasurface for multifunctional radiation and scattering modulation," *Optics Express*, Vol. 33, No. 2, 2047–2059, 2025.

[29] Yang, J., Z. Xu, J. Xin, and Z. Song, "Temperature-assisted terahertz reconfigurable metasurface for multi-polarization holographic display and encryption," *Optics & Laser Technology*, Vol. 181, 111968, 2025.

[30] Haimov, T., K. Aydin, and J. Scheuer, "Reconfigurable holograms using VO_2-based tunable metasurface," *IEEE Journal of Selected Topics in Quantum Electronics*, Vol. 27, No. 1, 1–8, 2021.

[31] Intaravanne, Y. and X. Chen, "Recent advances in optical metasurfaces for polarization detection and engineered polarization profiles," *Nanophotonics*, Vol. 9, No. 5, 1003–1014, 2020.

[32] Wen, D., F. Yue, G. Li, G. Zheng, K. Chan, S. Chen, M. Chen, K. F. Li, P. W. H. Wong, K. W. Cheah, *et al.*, "Helicity multiplexed broadband metasurface holograms," *Nature Communications*, Vol. 6, No. 1, 8241, 2015.

[33] Yan, T., Q. Ma, S. Sun, Q. Xiao, I. Shahid, X. Gao, and T. J. Cui, "Polarization multiplexing hologram realized by anisotropic digital metasurface," *Advanced Theory and Simulations*, Vol. 4, No. 6, 2100046, 2021.

[34] Zhang, L., H. Wang, Q. Jiang, L. Han, X. Zhang, and S. Zhuang, "Dual-wavelength multiplexed metasurface holography based on two-photon polymerization lithography," *Nanophotonics*, Vol. 14, No. 5, 581–588, 2025.

[35] Zhao, T., Y. Wu, Y. Xing, Y. Wang, J. Wu, and W. Zhou, "Design of the polarization-independent wavelength multiplexing holographic metasurface," *Photonics*, Vol. 10, No. 2, 139, 2023.

[36] Yin, Y., Q. Jiang, H. Wang, J. Liu, Y. Xie, Q. Wang, Y. Wang, and L. Huang, "Multi-dimensional multiplexed metasurface holography by inverse design," *Advanced Materials*, Vol. 36, No. 21, 2312303, 2024.

[37] Ye, W., F. Zeuner, X. Li, B. Reineke, S. He, C.-W. Qiu, J. Liu, Y. Wang, S. Zhang, and T. Zentgraf, "Spin and wavelength multiplexed nonlinear metasurface holography," *Nature Communications*, Vol. 7, No. 1, 11930, 2016.

[38] Deng, J., Y. Yang, J. Tao, L. Deng, D. Liu, Z. Guan, G. Li, Z. Li, S. Yu, G. Zheng, *et al.*, "Spatial frequency multiplexed meta-holography and meta-nanoprinting," *ACS Nano*, Vol. 13, No. 8, 9237–9246, 2019.

[39] Wang, J., J.-Y. Yang, I. M. Fazal, N. Ahmed, Y. Yan, H. Huang, Y. Ren, Y. Yue, S. Dolinar, M. Tur, and A. E. Willner, "Terabit free-space data transmission employing orbital angular momentum multiplexing," *Nature Photonics*, Vol. 6, No. 7, 488–496, 2012.

[40] Ren, H., G. Briere, X. Fang, P. Ni, R. Sawant, S. Héron, S. Chenot, S. Vézian, B. Damilano, V. Brändli, S. A. Maier, and P. Genevet, "Metasurface orbital angular momentum holography," *Nature Communications*, Vol. 10, No. 1, 2986, 2019.

[41] Fang, X., H. Ren, and M. Gu, "Orbital angular momentum holography for high-security encryption," *Nature Photonics*, Vol. 14, No. 2, 102–108, 2020.

[42] Jin, L., Y.-W. Huang, Z. Jin, R. C. Devlin, Z. Dong, S. Mei, M. Jiang, W. T. Chen, Z. Wei, H. Liu, *et al.*, "Dielectric multimomentum meta-transformer in the visible," *Nature Communications*, Vol. 10, No. 1, 4789, 2019.

[43] Li, J., P. Yu, S. Zhang, and N. Liu, "Electrically-controlled digital metasurface device for light projection displays," *Nature Communications*, Vol. 11, No. 1, 3574, 2020.

[44] Zhu, S., Z. Xu, H. Zhang, K. Yang, N. Wang, H. Liu, Y. Wang, J. Xia, and L. Huang, "Liquid crystal integrated metadevice for reconfigurable hologram displays and optical encryption," *Optics Express*, Vol. 29, No. 6, 9553–9564, 2021.

[45] Kaissner, R., J. Li, W. Lu, X. Li, F. Neubrech, J. Wang, and N. Liu, "Electrochemically controlled metasurfaces with high-contrast switching at visible frequencies," *Science Advances*, Vol. 7, No. 19, eabd9450, 2021.

[46] Liu, X., Q. Wang, X. Zhang, H. Li, Q. Xu, Y. Xu, X. Chen, S. Li, M. Liu, Z. Tian, *et al.*, "Thermally dependent dynamic meta-holography using a vanadium dioxide integrated metasurface," *Advanced Optical Materials*, Vol. 7, No. 12, 1900175, 2019.

[47] Zhang, F., X. Xie, M. Pu, Y. Guo, X. Ma, X. Li, J. Luo, Q. He, H. Yu, and X. Luo, "Multistate switching of photonic angular momentum coupling in phase-change metadevices," *Advanced Materials*, Vol. 32, No. 39, 1908194, 2020.

[48] Li, J., Y. Chen, Y. Hu, H. Duan, and N. Liu, "Magnesium-based metasurfaces for dual-function switching between dynamic holography and dynamic color display," *ACS Nano*, Vol. 14, No. 7, 7892–7898, 2020.

[49] Dong, L., Y. Li, J. Wei, and L. Zhu, "Four-channel holographic metasurface based on frequency-angle multiplexing," *Physica Scripta*, Vol. 99, No. 5, 055524, 2024.

[50] Kamali, S. M., E. Arbabi, A. Arbabi, Y. Horie, M. Faraji-Dana, and A. Faraon, "Angle-multiplexed metasurfaces: Encoding independent wavefronts in a single metasurface under different illumination angles," *Physical Review X*, Vol. 7, No. 4, 041056, 2017.

[51] Jang, J., G.-Y. Lee, J. Sung, and B. Lee, "Independent multichannel wavefront modulation for angle multiplexed metaholograms," *Advanced Optical Materials*, Vol. 9, No. 17, 2100678, 2021.

[52] Bao, Y., Y. Yu, H. Xu, Q. Lin, Y. Wang, J. Li, Z.-K. Zhou, and X.-H. Wang, "Coherent pixel design of metasurfaces for multidimensional optical control of multiple printing-image switching and encoding," *Advanced Functional Materials*, Vol. 28, No. 51, 1805306, 2018.

[53] Wang, E., J. Niu, Y. Liang, H. Li, Y. Hua, L. Shi, and C. Xie, "Complete control of multichannel, angle-multiplexed, and arbitrary spatially varying polarization fields," *Advanced Optical Materials*, Vol. 8, No. 6, 1901674, 2020.